WIND ENERGY SCIENCE

Realistic turbulent inflow conditions for estimating the performance of a floating wind turbine

Cédric Raibaudo[1,2]**, Jean-Christophe Gilloteaux**[1]**, and Laurent Perret**[1]

[1]Laboratoire LHEEA, UMR 6598, CNRS, Nantes Université, Centrale Nantes, 44321 Nantes, France
[2]Université d'Orléans, INSA-CVL, PRISME, EA 4229, 45072 Orléans, France

Correspondence: Laurent Perret (laurent.perret@ec-nantes.fr)

Abstract. A novel method for generating turbulent inflow boundary conditions for aeroelastic computations is proposed, based on interfacing hybrid hot-wire and particle image velocimetry measurements performed in a wind tunnel to a full-scale load simulation conducted with FAST. This approach is based on the use of proper orthogonal decomposition (POD) to interpolate and extrapolate the experimental data onto the numerical grid. The temporal dynamics of the temporal POD coefficients is driven by the high-frequency hot-wire measurements used as input for a lower-order model built using a multi-time-delay linear stochastic estimation (LSE) approach. Being directly extracted from the data, the generated three-component velocity fields later used as inlet conditions present correct one- and two-point spatial statistics and realistic temporal dynamics. Wind tunnel measurements are performed at a scale of 1 : 750, using a properly scaled porous disk as a floating wind turbine model. The motions of the platform are imposed by a linear actuator. Between all 6 degrees of freedom (DOFs) possible, the present study focus on the streamwise direction motion of the model (surge motion). The POD analysis of the flow, with or without considering the presence of the surge motion of the model, shows that a few modes are able to capture the characteristics of the most energetic flow structures and the main features of the wind turbine wake, such as its meandering and the influence of the surge motion. The interfacing method is first tested to estimate the performance of a wind turbine in an offshore boundary layer and then those of a wind turbine immersed in the wake of an upstream wind turbine subjected to a sinusoidal surge motion. Results are also compared to those obtained using the standard inflow generation method provided by TurbSim available in FAST.

1 Introduction

In recent years, floating offshore wind turbines (FOWTs) have been of particular importance for both scientific and industrial applications. Mounted on a floating structure, these turbines can be installed in deep waters, with more available space and power compared with onshore and fixed offshore wind turbines (Cruz and Atcheson, 2016). Understanding wind turbines' wakes is crucial to improve their aerodynamics when operating in farms (Schmidt and Stoevesandt, 2015; Bastine et al., 2018). For FOWTs embedded in farms, multi-dynamics and multi-scale phenomena can impact the wake characteristics and, therefore, the farm performance (Huang et al., 2018). In particular, the wake interaction be-

tween FOWTs significantly affects the power produced by the farms and needs to be considered carefully (Huang et al., 2018).

For the modeling and the prediction of the wind turbine wake, simplified analytic models have been suggested based mostly on the mean velocity deficit (Jensen, 1983; Frandsen et al., 2006; Bastankhah and Porté-Agel, 2014). These models could lack precision but are easier to compute compared with high-cost simulations, especially for wind farm control. Other parameters, such as the turbulence intensity, the geometrical properties (turbine diameter D, position in the wake x/D, roughness length z_0, etc.) and the thrust, can be included in the models for better representativeness (see the review of Kaldellis et al., 2021, for more details).

Porous disks have been used as surrogate wind turbines in wind turbine studies. This approach is similar to the actuator disk theory used for the theoretical and numerical prediction of wind turbine performance, in which the rotor is replaced by a permeable disk generating an equivalent thrust (Betz, 1920; Joukowsky, 1920). The pioneer study of Aubrun et al. (2013) showed that the mean velocity deficit, the integral scales and the statistics of the porous disk wake are similar to those of a model with a rotor for downstream positions in the wake $x/D > 3$. Similar conclusions were found by Camp and Cal (2016) for $x/D > 3.5$. Porous disks are therefore valid for the characterization of the far-field wake, where, in farms, other downstream wind turbines are expected to be located (Porté-Agel et al., 2020).

Unsteady phenomena occur in the wind turbine wake, in particular wake meandering. Meandering is a large-scale motion of the wake due to the interaction between the rotor and large coherent structures of the incoming boundary layer (Porté-Agel et al., 2020; Hodgkin et al., 2023). Meandering is also sensitive to the incoming flow conditions, such as the turbulence level (Foti et al., 2018; Porté-Agel et al., 2020). The physical mechanism of this phenomenon is still not fully understood and continues to be an object of study.

For FOWTs, the unsteady behavior of the wake interacts with the wave-induced motion of the platform. Rockel et al. (2014) first studied the effect of one of the motion components – the pitch – on the wake dynamics using stereoscopic particle image velocimetry (PIV). Their study showed that the motion creates additional vertical velocity and reduces the kinetic energy available for a downwind turbine. Khosravi et al. (2015) considered the surge motion and observed a slowdown of the wake recovery and a decrease in the kinetic energy, but they also noted a 1 % increase in the power produced for the given turbine. By considering pitch and roll experimentally, Fu et al. (2019) showed no effect of the motions on the mean power produced. However, the pitch motion reduces the power fluctuations in the lowest-frequency part of the spectrum, for frequencies lower than the imposed pitch motion harmonics. The roll motion also reduces these fluctuations around a specified frequency, about half of the motion main harmonics. On the other hand, Corniglion et al. (2020) observed the effect of a high-frequency surge motion, in particular an increase in the mean thrust and the axial velocity in the wake. Recent works (Messmer et al., 2022; Fontanella et al., 2022; Chen et al., 2022; Li et al., 2022) have investigated the effect of more complex motions on the wake dynamics, in particular the meandering. However, these effects are still not fully understood for floating wind turbines. The difficulties with respect to understanding these effects increase when considering realistic atmospheric conditions for numerical and experimental studies. By varying the turbulence intensity of the incoming flow, significant differences in the wake properties and/or the power produced by the wind turbine can be observed (Saranyasoontorn and Manuel, 2005; Chamorro and Porté-Agel, 2009; Nybø et al.,

2020). Other studies (Chamorro and Porté-Agel, 2009; Bastine et al., 2014; Schliffke, 2022) have taken into account a significant atmospheric turbulent boundary layer upstream of the wind turbine. In particular, the axisymmetry of the incoming flow plays an important role in the redistribution of the turbulence levels in the turbine wake (Chamorro and Porté-Agel, 2009).

As explained in the two previous paragraphs, considering realistic conditions for the incoming flow and wave-induced motions is crucial to estimate the performance of floating wind turbines. It is also clear today that atmospheric turbulence cannot be treated as a purely random phenomenon characterized only by its intensity. To address this problem, the strategy commonly used in the wind energy community is based on the generation of synthetic turbulence with a target spectral content representative of the atmosphere (Kelley and Jonkman, 2007; Mann, 1998). This approach, implemented in the TurbSim turbulence generator of the FAST aeroelastic code of the National Renewable Energy Laboratory (NREL), has been improved to account for particular phenomena such as low-level jets or Kelvin–Helmholtz instabilities that can develop in the atmosphere under certain conditions (Kelley and Jonkman, 2007). In the case of wind farm studies, the turbines are located in the wake of other machines; thus, the synthetic turbulence approach can no longer be used directly and must be modified to take into account the presence of the wake so as to perform aeroelastic calculations under realistic conditions. The developed approaches range from simple wake models imposing an additional velocity deficit to stochastic wake models based on large-eddy simulation (LES)-type precursor computations through intermediate models considering the velocity deficit as well as the meandering of the wake (see Bastine et al., 2018, and references therein).

In the context of the LES computation of turbulent flows, Perret et al. (2006, 2008) proposed an alternative method to generate realistic unsteady inflow conditions by coupling wind tunnel measurements to an LES code to simulate a turbulent mixing layer flow. In their approach, non-time-resolved stereoscopic PIV measurements were performed in a cross-section of the flow corresponding to the inlet section of the targeted LES simulation. Using proper orthogonal decomposition (POD) to decompose the velocity fields into a set of spatial modes and temporal coefficients, a low-order representation of the flow was built. The time evolution of the temporal coefficients was modeled either in a purely stochastic manner via random Gaussian numbers with a realistic spectrum (Perret et al., 2006) or by deriving a low-order dynamic model of the temporal evolution of the most energetic structures (Perret et al., 2008). The incoherent motion was modeled by employing time series of Gaussian random numbers to mimic the temporal evolution of higher-order POD modes. Beyond the fact that this innovative method allows for the study of complex flow configurations (as long as wind tunnel measurement can be performed), it enables the

generation of inlet conditions with a realistic spatiotemporal organization, a feature often missing in purely stochastic approaches.

Building upon the work of Perret et al. (2006, 2008), the present study aims to propose a novel approach based on a direct coupling between experimental data from a scaled-down wind tunnel experiment and a full-scale load computational code (FAST from NREL in the present case). The methodology is applied on experimental data representative of a FOWT model under surge motion and realistic conditions of the incoming flow. As detailed in the following, it relies on stereoscopic PIV performed in a cross-section of the wind turbine wake combined with the derivation of a data-driven low-order model to improve the temporal dynamics of the PIV measurements. This database of temporally well-resolved vector fields generated in the cross-section of the flow are then used as unsteady inlet conditions for the load computation. After a description of the experimental setup (Sect. 2), details on the scaling between the model and a real-scale prototype will be discussed (Sect. 3). The flow without a model and the mean wake are then presented (Sect. 4). The velocity fields are reconstructed at a high sampling frequency using stochastic estimation (Sect. 5) before being coupled to FAST simulations to evaluate the power produced by a down-wind floating wind turbine submitted to the wake under surge motion (Sect. 6).

2   Experimental setup

Experiments were carried in the LHEEA (Laboratoire de recherche en Hydrodynamique, Énergétique et Environnement Atmosphérique) laboratory's atmospheric wind tunnel. Without a model, the freestream velocity of the wind is $U_\infty = 4.2\,\mathrm{m\,s^{-1}}$ and its turbulent intensity far from the wall is about 0.5 %. The experimental setup is presented in Fig. 1. The wind turbine is modeled using a porous disk with a diameter of $D = 0.16\,\mathrm{m}$. The disk's center is set at a height $z_\mathrm{hub} = 0.12\,\mathrm{m}$ with respect to the floor. The model represents the floating 2 MW wind turbine used in the FLOATGEN research project, installed at Centrale Nantes' offshore test site in Le Croisic, France (Rousset et al., 2010). The thrust coefficient C_t is estimated to be approximately 0.65 and the power coefficient $C_\mathrm{p} \approx 0.25$ (Schliffke et al., 2020). For streamwise positions x/D in the wake further than 3, the use of porous disks for the characterization of wind turbine wakes is considered valid (Schliffke et al., 2020). The thickness of the incoming boundary layer is $\delta = 0.6\,\mathrm{m}$ and the resulting Reynolds number is $Re = U_\infty \delta / \nu \approx 160\,000$.

To replicate realistic behaviors of floating wind turbines under wave swell, a sinusoidal surge motion is imposed on the model using a linear actuator (Schliffke et al., 2020). The setup to model this motion is presented in Fig. 2. The sinusoidal amplitude is $\pm 0.01\,\mathrm{m}$ and the frequencies tested are $f_\mathrm{m} = [0,\ 2,\ 3,\ 3.75]\,\mathrm{Hz}$. Using the incoming velocity speed

and the disk diameter, this corresponds to a nondimensionalized frequency of $F_\mathrm{m}^+ = f_\mathrm{m} D / U_\infty = [0,\ 0.08,\ 0.11,\ 0.14]$. The model position is controlled retroactively and monitored, with a bias of about 1 mm between the expected and real positions (Schliffke et al., 2020). As indicated in Fig. 2, the variable x axis corresponds to the flow direction; the y–z plane is normal to the flow. The coordinates' origin is chosen at the disk center.

Instantaneous three-component velocities of the wake were acquired using stereoscopic PIV in a y–z plane normal to the main flow direction at two streamwise positions, $x/D = 4.6$ and 8.1, downstream of the wind turbine model. Two 2560 pixels $\times$ 2160 pixels Zyla sCMOS cameras (Oxford Instruments) were set up upstream on each side of the wind tunnel. Nikon lenses with a focal length of $f_\mathrm{o} = 60\,\mathrm{mm}$ were fixed on the cameras. Scheimpflug adapters were used to ensure a focused image over the full field of view. The laser sheet was generated using a double-pulse Nd:YAG laser (200 mJ per cavity). A LaVision Laskin nozzle aerosol generator was used to seed the flow with olive oil droplets of 1 µm diameter. Transparent film was added at the walls to reduce the light diffusion. The time delay between the two pulses was $dt_\mathrm{PIV} = 300\,\mu\mathrm{s}$. Image analysis was performed using a standard cross-correlation multi-pass algorithm with a final interrogation window size of $32 \times 32\,\mathrm{px}^2$ using Dantec Dynamics software. The size of the final region of interest was about $3\,D \times 2\,D$. The sampling frequency was $f_\mathrm{PIV} = 14.1\,\mathrm{Hz}$, and 14 000 snapshots were acquired for each case. The number of snapshots was doubled for one case to estimate the statistical convergence.

Constant temperature anemometry (CTA) measurements were also performed simultaneously with the PIV. A total of 12 hot-wire (HWA) sensors were distributed spanwise downstream of PIV measurement plane and at two heights (0.47 and 1.25 D). The sampling frequency for the sensors was $f_\mathrm{HWA} = 15\,\mathrm{kHz}$. Sensors were calibrated using King's law by measuring the free streamflow with the help of a Pitot tube. The calibration procedure and the post-processing of the raw voltages accounted for temperature correction using the method proposed by Hultmark and Smits (2010).

3   Scaling

The experimental setup presented in the previous section was chosen to respect scaling properties between the model and the chosen prototype. A complete study on how to scale wind turbines rotors was developed by Canet et al. (2021), for example, and a full explanation of the scaling methodology for the present case can be found in Schliffke (2022). As the numerical model of the FLOATGEN prototype or its detailed characteristics are not available for the FAST simulations due to confidentiality constraints, a 5 MW reference wind turbine is used (Jonkman et al., 2009). The full-scale rotor diameter is $D_\mathrm{P} = 120\,\mathrm{m}$, the hub height is $z_{0,\mathrm{P}} = 90\,\mathrm{m}$, the atmo-
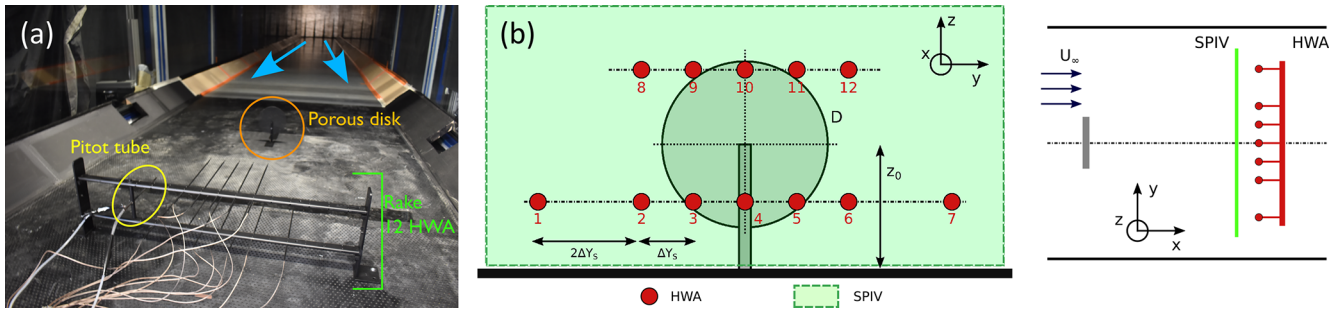
Figure 1. Experimental setup: **(a)** picture of the setup in the wind tunnel and **(b)** schemes of the metrology setup.
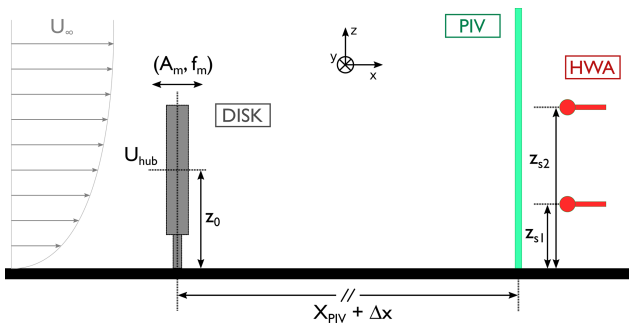

Figure 2. Sketch of the surge motion experimental setup.

spheric boundary layer is about $\delta \approx 300$ m and the incoming velocity at the hub height is $U_{0,P} = 10$ m s^{-1}, also corresponding to the parameter implemented in the present FAST simulations.

Therefore, scaling factors are determined between the model and the NREL reference wind turbine. First, the geometric scaling factor based on the rotor diameter is $\Lambda_L = D_P/D = 750$. The porous disk diameter is chosen to respect a blocking factor of 0.5 %, which is under the 5 % required by guideline 3783 of the Association of German Engineers (VDI; VDI, 2017). The model hub height is fixed at $z_0 = 0.12$ m to be totally immersed in the boundary layer, which has a height of $\delta = 0.6$ m. It corresponds to the NREL hub height of 90 m immersed in atmospheric boundary layers with height values of between 300 and 500 m. The integral scale of the flow is about 0.4 m, corresponding to an integral scale of 200 m for the full scale, also respecting the VDI guidelines (VDI, 2017; Schliffke, 2022).

The velocity scaling factor is defined using the hub velocity by $\Lambda_V = U_{hub,P}/U_{hub}$. The standard objective for FAST simulations is $U_{hub,P} = 10$ m s^{-1}. For the model, for a freestream velocity of $U_\infty = 4.2$ m s^{-1}, the velocity at the hub height in the undisturbed oncoming boundary layer is $U_{hub} = 3.8$ m s^{-1}. The scaling factor is therefore $\Lambda_V = 2.6$. Using Strouhal number similarity, the time scaling factor is $\Lambda_t = \frac{\Lambda_L}{\Lambda_V} = 284$. This means a physical phenomena in the wind tunnel occurs 284 faster than for the prototype. For the FAST implementation with this time factor, to simulate the

aerodynamics at a classical sampling frequency of around 20 Hz, velocity fields are needed at a minimal frequency of 5680 Hz. Reconstruction of the velocity fields at a frequency higher than that of the PIV measurements is therefore necessary.

The displacement system has been designed to replicate measurements performed on the SEM-REV test site where the FLOATGEN prototype. The design justification is fully explained in Schliffke (2022), based on the study of Tarpin (2018). The most probable sea state is of height $H_S = 4.6$ m and characteristic wave period $T_P = 11$ s. Considering the wind turbine properties, this leads to a most probable wave motion of $F^+ = 0.7$. However, as explained by Schliffke (2022), the operating frequency range is between $F^+ = 0.4$ and 3.2. Therefore, the chosen actuator frequencies are low compared with the expected wave motion of the full-scale wind turbine. However, the actuator frequencies' range covers part of the low-frequency range of the natural frequencies and is of the same order of magnitude as the expected phenomena.

4   Mean structure of the flow

The turbulent boundary layer without a model is first documented with the present experimental campaign. Only the main elements of the flow without a model are presented here, but more details can be found in previous works (Perret et al., 2006, 2008; Schliffke et al., 2020; Raibaudo and Perret, 2022). Mean and root-mean-square (RMS) velocities of the atmospheric turbulent boundary layer without a model are presented in Fig. 3. Profiles of the three components along the wall-normal direction z/D going through the disk center ($y/D = 0$) are considered here. Mean streamwise velocity $\overline{U}/U_\infty$ corresponds to a classical turbulent boundary layer profile. Near the wall, the RMS streamwise velocity reaches $\sigma_u/U_\infty = 0.082$, leading to a maximum turbulence level of $I_u = \sigma_u/\overline{U} \approx 13$ %. A small negative spanwise velocity $\overline{V}/U_\infty \approx 0.01$ is also observed in the figure. This has been observed in previous works and could be linked to large flow structures developing upstream of the measurement region.
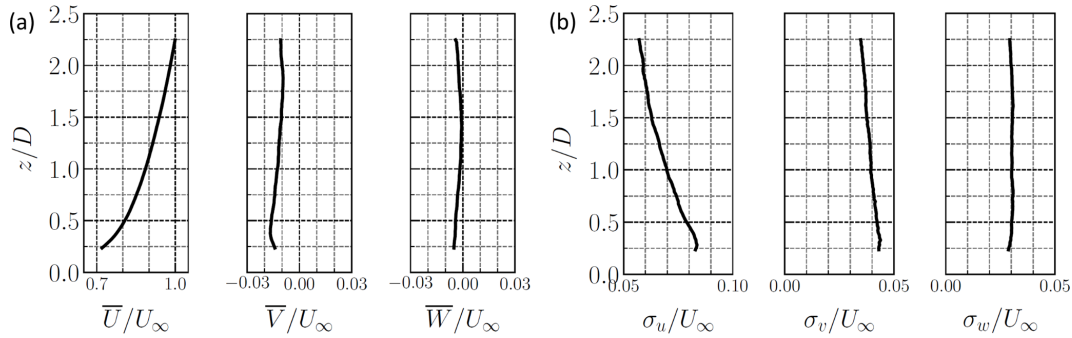
Figure 3. Mean $\overline{U}/U_\infty$ **(a)** and RMS velocities $\sigma_\mathrm{u}/U_\infty$ **(b)** at $y/D = 0$ for the three velocity components for the turbulent boundary layer without a model. Note that different scales were chosen between the streamwise velocity and the other velocity components.
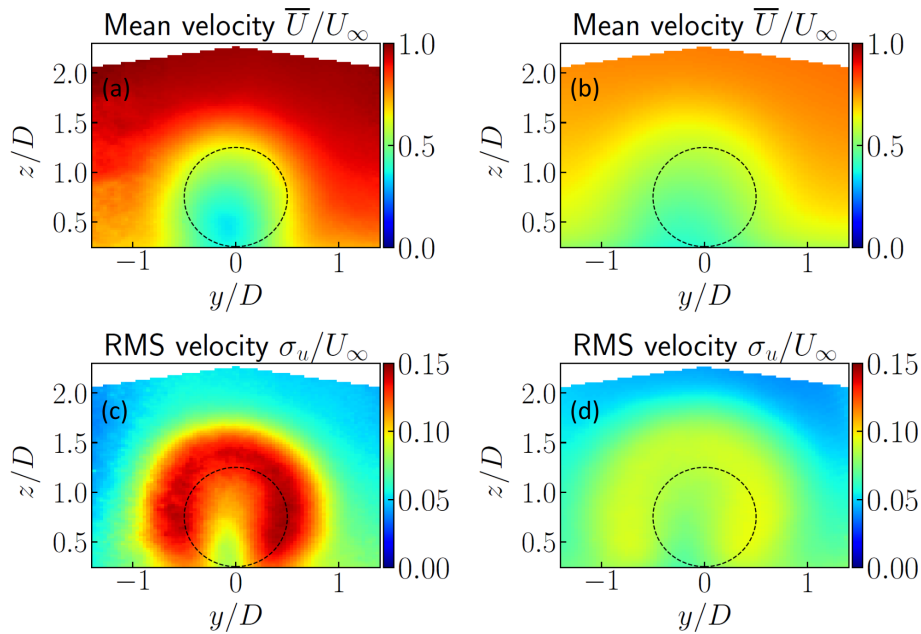

Figure 4. Streamwise mean $\overline{U}/U_\infty$ **(a, b)** and RMS velocity $\sigma_\mathrm{u}/U_\infty$ **(c, d)** for **(a)** the wake for the fixed model at $x/D = 4.6$ and **(b)** the wake for the fixed model at $x/D = 8.1$. Dashed lines correspond to the position of the porous disk in the y–z plane.

The mean wake flow is then presented here. Streamwise mean and RMS velocity fields are presented in Fig. 4. Two streamwise positions in the wake are presented here: $x/D = 4.6$ and 8.1. The mean flow in the near-wake region is disturbed by the disk, following its shape (represented using a dashed line in Fig. 4). At $x/D = 8.1$, the wake center is slightly shifted in the negative y direction, as also seen in previous works (Schliffke et al., 2020; Foti et al., 2019). This could correspond to the small spanwise velocity of the incoming flow observed previously (Raibaudo and Perret, 2022). Compared with the flow without a model, the turbulence intensity increases in the near-wake region from 8 % up to 15 %. The circular horseshoe shape in the near-wake region has been found in previous works (Hamilton et al., 2018). The slight shift in the negative y direction is observed in the RMS fields at $x/D = 8.1$. It must be noted here that, at

the most downstream location $x/D = 8.1$, two distinct peaks in the horizontal profile of the RMS of the streamwise velocity component measured at the hub height are still visible, indicating that the wake is not yet fully developed. However, the recovery of the mean velocity $u(z = z_\mathrm{hub})/U_\mathrm{hub}$ reaches 60 % of the undisturbed velocity, with a corresponding decreasing turbulent intensity. The wake is therefore still in its transition phase towards a fully developed wake. More details on the mean flow can be found in Schliffke et al. (2020) and Belvasi et al. (2022).

5 Stochastic reconstruction using POD–linear stochastic estimation (LSE) multi-delays

For the coupling of wind tunnel PIV velocity fields with an aeroelastic code to perform a full-scale load simulation,

due to the scaling constraints presented in Sect. 3, a high-sampling frequency is required. By combining the velocity fields acquired with PIV and time-resolved HWA measurements, stochastic approaches are used here to reconstruct velocity fields at a high temporal resolution.

5.1 Methodology

Reconstruction of the velocity fields is performed using a proper orthogonal decomposition and multi-time-delay linear stochastic estimation (POD–mLSE) approach (Durgesh and Naughton, 2010), which is an extension of the standard POD–LSE technique developed by Bonnet et al. (1994). Velocity fields are first decomposed into temporal and spatial modes using the standard snapshot POD (Sirovich, 1987):

$$\boldsymbol{u}(\boldsymbol{x}, t) \approx \sum_{i=0}^{N_{\mathrm{m}}} a_i(t) \Phi_i(\boldsymbol{x}), \tag{1}$$

where N_{m} is the number of modes selected for the truncation. The POD procedure is not fully detailed here, but the main elements are summarized now. A kernel $\boldsymbol{\kappa}$ is build from the snapshots' matrix $\mathbf{U}_{\mathrm{s}}$ corresponding to the velocity fields reorganized as 1D vectors for each time: $\boldsymbol{\kappa} = \mathbf{U}_{\mathrm{s}}^T \mathbf{U}_{\mathrm{s}}$. The square matrix $\boldsymbol{\kappa}$ is therefore inverted to solve an eigenvalue problem:

$$\boldsymbol{\kappa} \mathbf{A}_i = \lambda_i \mathbf{A}_i, \tag{2}$$

where λ_i represents the eigenvalues and $\mathbf{A}_i$ denotes the temporal modes matrix in which the temporal modes a_i are extracted. After a descending sort by eigenvalue amplitude, the spatial modes Φ_i are obtained as follows:

$$\Phi_i = \mathbf{A}_i \mathbf{U}_{\mathrm{s}} / \|\mathbf{A}_i \mathbf{U}_{\mathrm{s}}\|. \tag{3}$$

Here, $N_{\mathrm{m}} = 100$ modes are chosen, corresponding to about 80 % of the cumulative eigenvalues' energy. The objective of the stochastic estimation is to determine the more suitable coefficients B_{ijk} to express the relation between the temporal modes a_i and the HWA sensors with time delays τ_k. The reconstructed temporal modes $\widehat{a}_i$ are then estimated at a higher sampling rate:

$$\widehat{a}_i(t) = \sum_{j=0}^{N_j} \sum_{k=0}^{N_k} B_{ijk} S_j(t - \tau_k), \tag{4}$$

where $N_j = 12$ is the number of HWA sensors S_j and N_k is the number of delays imposed on the sensors. Here, $N_k = 21$ delays are distributed within ± 0.2 s, following comparable reconstruction parameters on similar experiments (Blackman and Perret, 2016). The coefficients B_{ijk} are determined through the resolution of a least-squares minimization problem using cross-correlations:

$$B_{ijk} = \mathbf{C}_{\{a_i, S_{jk}\}}^{-1} \mathbf{C}_{\{S_{jk}\}}, \tag{5}$$

where $\mathbf{C}_{\{a_i, S_{jk}\}}$ represents the cross-correlations between the temporal modes and the sensors with delays and $\mathbf{C}_{\{S_{jk}\}}$ represents the correlations between the different sensors with different delays. Temporal modes $\widehat{a}_i$ are therefore estimated at a higher temporal resolution using Eq. (4) and then combined with the spatial modes using POD (Eq. 1) to reconstruct the velocities. Only results for the downstream location $x/D = 8.1$ are presented here, which corresponds to the inlet section of the load simulations. The sampling frequency used for the reconstruction is $f_{\mathrm{s}} = 7.05$ kHz, to meet the conditions required for these simulations.

5.2 Proper orthogonal decomposition

A selected set of results from the POD analysis are presented here, but more details can be found in previous works from the authors (Raibaudo et al., 2022).

The convergence using the cumulative eigenvalues $\sum_{i}^{N_{\mathrm{m}}} \lambda_i / \sum_{i}^{\infty} \lambda_i$ is first shown in Fig. 5. The two streamwise positions in the wake are considered and are compared with the POD modes for the turbulent boundary layer without a model. Compared with typical bluff-body flows, the eigenvalues' convergence is slow, due to the high Reynolds number of the incoming turbulent boundary layer. For comparison, only the first modes concentrate the energy for bluff bodies (53 % of the total fluctuations energy in the two first modes for the square cylinder wake of Leite et al., 2018, for example). The eigenvalues are therefore comparable with previous works, in particular De Cillis et al. (2021): for a near-wake flow downstream of a nacelle and tower model, the cumulative eigenvalues reached about 40 % after $N_{\mathrm{m}} = 15$ modes, whereas it is about 50 % for the present study for the same number of modes.

Spatial POD modes obtained from the database are first presented here. This corresponds to the analysis performed in Raibaudo et al. (2022). In particular, maps of the spatial modes of the streamwise velocity component Φ_U for $x/D = 8.1$ and profiles along the spanwise y direction and for two streamwise positions are presented in Fig. 6. Profiles are considered at the hub height ($z/D = 0.74$) and for different frequencies of surge motion. Modes' signs are adapted for a better comparison. A more complete analysis of the POD modes for the floating wind turbine can be found in Raibaudo et al. (2022). Two salient features can be observed from it: (i) the structure of the spatial modes forming around the disk shape are similar to previous works on POD analysis on wind turbines wakes (Bastine et al., 2015) and (ii) no significant effect of the surge motion can be found in the spatial modes. Modes' profiles are close in amplitude and shape, shown here for the streamwise velocity modes as well as for the other velocity components $\boldsymbol{v}$ and $\boldsymbol{w}$.

However, significant differences can be observed in the temporal modes. The premultiplied power spectral density (PSD) of the temporal modes a_i is presented in Fig. 7 for
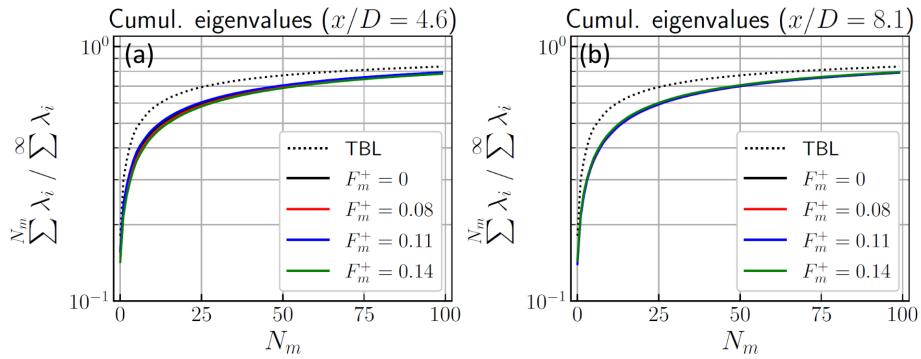
Figure 5. Cumulative eigenvalues $\sum^{N_m} \lambda_i / \sum^{\infty} \lambda_i$ from the POD obtained from different streamwise positions **(a)** $x/D = 4.6$ and **(b)** $x/D = 8.1$. For each configuration, four frequencies of surge motion F_m^+ are presented using solid lines: 0 (fixed), 0.08, 0.11 and 0.14. The turbulent boundary layer (TBL) without a model is presented using a dotted line.
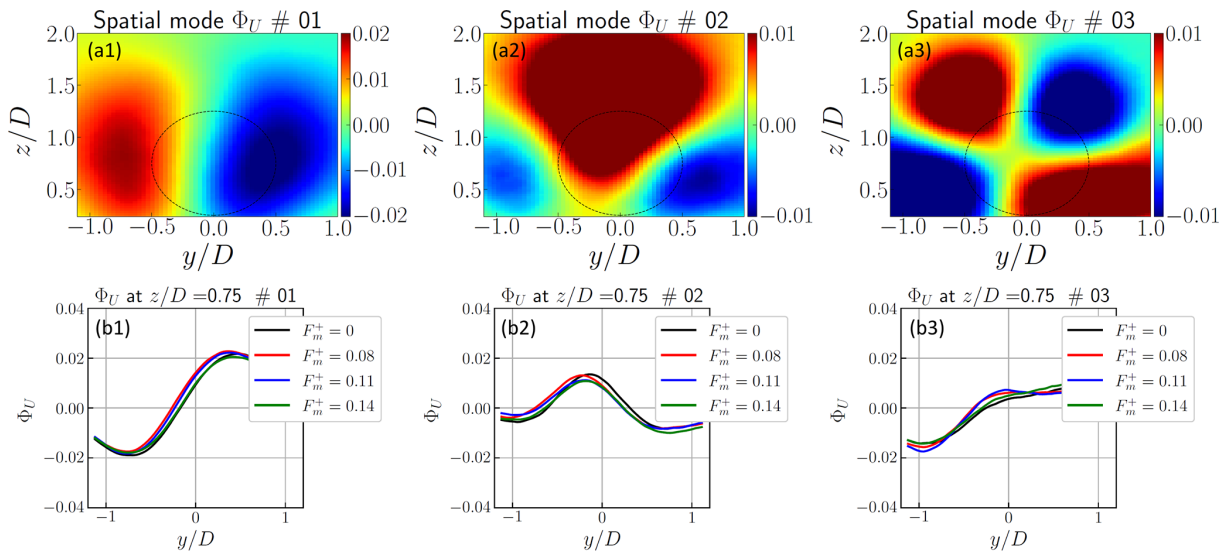

Figure 6. (a) Maps of spatial modes Φ_U for $x/D = 8.1$ for modes $i = 0$ to 2 and **(b)** profiles along the spanwise y direction at the hub height $z/D = 0.74$ with the effect of the surge motion (Raibaudo et al., 2022).

the turbulent boundary layer without a model and the two streamwise positions in the wake. Despite the low sampling rate of the PIV system, the surge motion imprint can be clearly identified.

A broad spectrum is found for the flow without a model, centered around the main reduced frequency at $f^+ = 0.04$ ($f \approx 1\,\mathrm{Hz}$). By considering the fixed porous disk wake, the spectra amplitude changes significantly and the main frequency is shifted to $f^+ = 0.13$ ($f \approx 3\,\mathrm{Hz}$). The surge motion is found to influence the temporal dynamics of the wake. The influence of the highest surge motion frequencies is significantly visible: the spectrum is similar between a motion at frequency $-F_m^+ = 0.08$ and the fixed model, where substantial peaks are observed for frequencies $F_m^+ = 0.11$ and 0.14. The difference between low and high frequencies is even more significant between modes 1 and 2: mode 1, especially in the far field, is mostly influence by the highest frequencies,

whereas mode 2 is impacted by all of the surge motion frequencies. As detailed in the following, this could be linked to a mitigation of the horizontal meandering and the downwash phenomenon, respectively.

5.3 Physical interpretation of the modes' dynamics

The relationship between the POD modes and the known physical phenomenon in wind turbine wakes is investigated by considering the dynamics of the location of the wake center. The methodology corresponds to that used by Bastine et al. (2015) and is employed to estimate the center of the wake deficit. Using the deficit velocity $\tilde{u}(\boldsymbol{x}, t) = U_0 - \boldsymbol{u}(\boldsymbol{x}, t)$, where U_0 is the local freestream velocity, the center coordinates are calculated as follows:
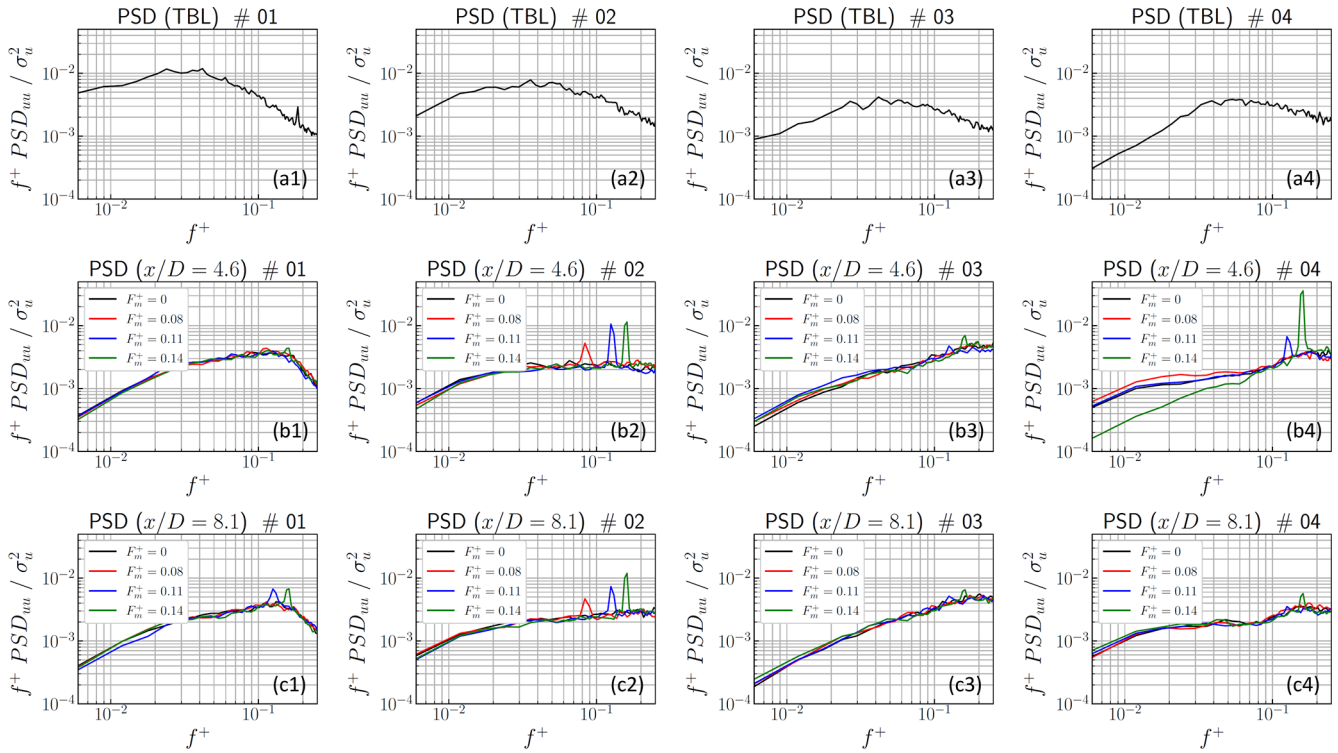
Figure 7. Premultiplied PSD of the temporal modes a_i obtained from different configurations: **(a)** TBL without a porous disk, **(b)** wake at $x/D = 4.6$ and **(c)** wake at $x/D = 8.1$. The numbers 1–4 in the panel labels represent modes 1 to 4, respectively.
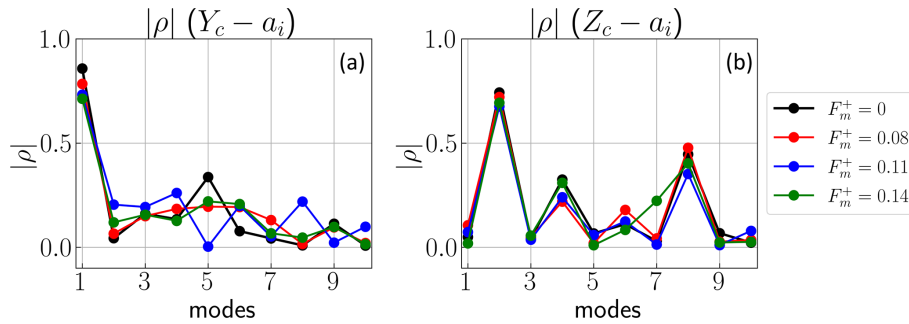

Figure 8. Absolute value of the Pearson correlation coefficients between the **(a)** spanwise and **(b)** wall-normal coordinates and the temporal POD modes.

$$\begin{bmatrix} y_c(t) \\ z_c(t) \end{bmatrix} = \frac{\iint \tilde{u}^2(y,z,t) \begin{bmatrix} y \\ z \end{bmatrix} \mathrm{d}y\mathrm{d}z}{\iint \tilde{u}^2(y,z,t)\mathrm{d}y\mathrm{d}z}. \tag{6}$$

Correlations of these coordinates with the POD temporal modes are presented in Fig. 8. Pearson's correlation coefficient is considered here for the wake at $x/D = 8.1$. Conclusions are similar to those found by Bastine et al. (2015). The first mode strongly correlates with the spanwise motion of the wake, suggesting that this mode corresponds to the horizontal meandering. The correlation decreases monotonically when the surge motion frequency increases, from $\rho(y_c, a_1) = 0.86$ for the fixed model to 0.71 for $F_m^+ = 0.14$.

This decrease in the correlation with mode 1 is counterbalanced on the next three modes. The second mode instead correlates better with the wall-normal wake motion, which could correspond to the downwash flow motion and the vertical meandering. The correlation coefficient also decreases, from $\rho(z_c, a_2) = 0.74$ to 0.68 for $F_m^+ = 0.11$. Contrary to y_c, correlation between the wall-normal position z_c and the modes reaches a maximum for modes 4 and 8. These higher modes are usually difficult to interpret, as they correspond to a combination of motions. However, for these modes 2, 4 and 8, the spatial modes' consistency (not shown here) is mostly due to the wall-normal velocity component and a vertical motion of the wake. Then, the correlation amplitude decreases for

the highest frequencies and for both the spanwise and wall-normal direction. This could correspond to a full mitigation of the wake coherence and flow dynamics.

5.4 Reconstruction using multi-time-delay LSE

Following the methodology for reconstruction in Sect. 5.1 and Eq. (4) in particular, the velocity fields are reconstructed at a high sampling rate using the HWA time-resolved sensors. RMS velocity profiles of the reconstructed velocities along z are shown in Fig. 9. A comparison between the reconstructed and original velocities is therefore necessary to validate the reconstruction. As $N_m = 100$ POD modes are used to reconstruct the velocity, the comparison is not done with the raw velocity profiles but rather with the original velocity reconstructed with the same number of modes.

For the turbulent boundary layer (Fig. 9a), the streamwise RMS velocity profile σ_u/U_∞ is well reconstructed and reaches 60 % of the original velocity. The other reconstructed components σ_v and σ_w are underestimated (around 40 % for the spanwise and 50 % for the wall-normal component), but they are still significant in amplitude. The same analysis can be made for the reconstruction of the wake flow (Fig. 9b). The RMS values of the reconstructed velocities are underestimated but show a similar spatial distribution. Even if the stochastic estimation loses information similarly to the turbulent boundary layer (TBL), this underestimation could be linked to the conditioning of the correlation matrix during the POD process. The inversion of this matrix could amplify the smaller eigenvalues for ill-conditioned LSE problems (Podvin et al., 2018). However, the differences between the projected and the reconstructed velocities are comparable to previous works using the same approach (Dekou et al., 2016; Podvin et al., 2018). Furthermore, the presence of the model generates a 3D wake which is well captured by the PIV but not well enough by the 1D hot-wires, which could also leads to errors.

Only the turbulent boundary layer and the far-wake for the fixed model are shown here, but the stochastic estimation was performed for the full database. By considering surge motion, as its impact on the mean quantities is limited, the reconstructed profiles are similar to those presented in Fig. 9b. For all of the cases, the reconstructed velocities are reduced in amplitude by the POD–LSE process, but their main properties are conserved.

A spectral analysis of the reconstructed streamwise velocity is presented in Fig. 10. Premultiplied PSD values of the reconstructed velocity are compared with those estimated from the original PIV velocity, truncated with the same number of POD modes, and with a hot-wire sensor located at $y/D = 0$ and $z/D = 1.25$ (no. 10 in Fig. 1). The spectrum of the reconstructed velocity is consistent at low frequency with the PIV and follows the dynamics behavior of the HWA sensor well. A loss of spectrum amplitude is also observed between the two, suggesting a loss of information at higher frequency with the stochastic reconstruction, as explained previously. Compared to the reconstructed turbulent boundary layer (Fig. 10a), the reconstructed wake shows peaks at a low frequency of around $f^+ = \mathcal{O}(10^{-1})$, which is consistent (as expected) with the spectral analysis performed on the temporal modes (Fig. 7).

6 FAST simulations using experimental velocities

Reconstructed velocity fields in the far field ($x/D = 8.1$) are now implemented as inflow wind conditions in FAST simulations, where the effect of the surge motion and the flow dynamics on the computed produced power are considered in the present study.

6.1 Methodology

Spatial processing of the PIV velocity fields is first needed to adapt the velocity fields to the FAST requirements. As the inflow wind conditions for FAST have to reach down to the floor, the spatial POD modes are first extrapolated to be equal to zero at the wall. Velocity fields are then reconstructed with these extrapolated modes by POD projection (Eq. 1). The spatial range is then reduced to $Y_{FAST} = \pm 0.56\,D$ and $Z_{FAST} = [0,\ 1.38\,D]$ in a region close to the disk position and down to the wall. Interpolation is also required to have a square grid and an equal number of points ($N_{p,y} = N_{p,z} = 31$). Finally, the velocity fields are scaled to set the hub velocity $U_{hub,P} = 10\,\mathrm{m\,s^{-1}}$. Even if these operations are significant, features of the flow are conserved, especially the reconstructed spatiotemporal dynamics of the flow obtained previously. All extrapolation and interpolation operations are performed using bivariate B-spline functions (Dierckx, 1981).

As a reference, generic turbulent velocity fields are also generated using TurbSim (Kelley and Jonkman, 2007), the turbulence generation tool provided with FAST. They correspond to velocity fields with prescribed boundary conditions and turbulence intensity, although without any coherence with respect to their dynamics. For the boundary layer, the power law exponent is $\alpha = 0.15$ and the surface roughness length is $z_r = 0.01\,\mathrm{m}$. Four turbulence intensity profiles are chosen for these fields: for the first three datasets, the turbulence intensities at the hub are set to 5 %, 7 % and 10 %. The last dataset follows the reference Normal Turbulence Model (NTM) in IEC 61400-1 requirements (International Electrotechnical Commission, 2006). Class C is chosen from this model, corresponding to the minimal turbulence class and a turbulence intensity of 12 % at the hub. The other parameters are the same as the fields from experiments ($U_{hub,P} = 10\,\mathrm{m\,s^{-1}}$, $N_{p,y} = N_{p,z} = 31$).

Simulations are performed using FAST, as implemented in the software QBlade (v0.963), developed by the Technical University of Berlin (Marten et al., 2015). The tip-speed ratio (TSR) is fixed at 6.6, under the optimal value of 8 for this wind turbine. The full-scale sampling frequency
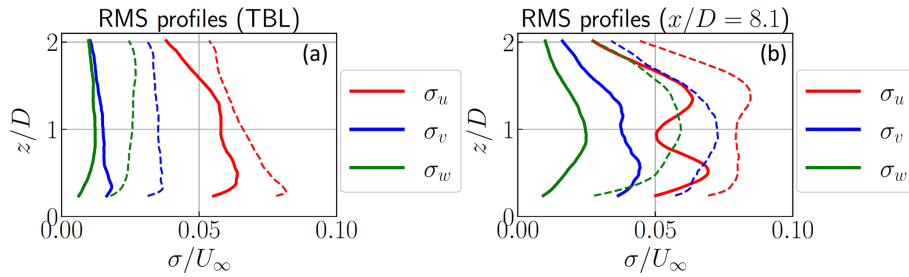
Figure 9. RMS reconstructed velocity u/U_∞ profiles along z using POD-mLSE and the original velocity using the same number of modes $N_m = 100$. Panels **(a)** and **(b)** show the TBL and the fixed model at $x/D = 8.1$, respectively. Dashed lines present the truncated original PIV data and solid lines show the POD-mLSE data.
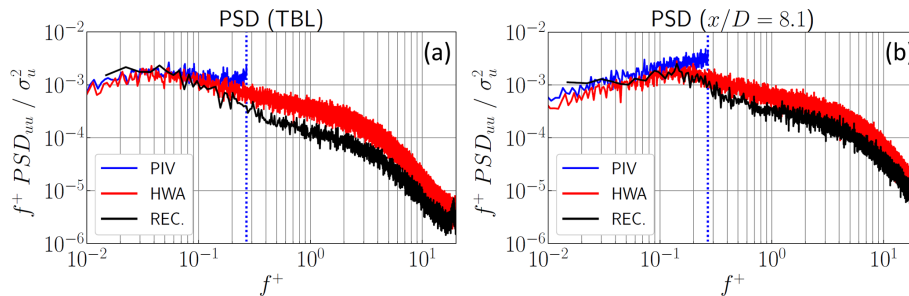

Figure 10. Premultiplied PSD of the reconstructed velocities at the hub height compared to that directly measured by PIV or HWA. Panels **(a)** and **(b)** show the TBL and the fixed model at $x/D = 8.1$, respectively. The vertical dashed line corresponds to the PIV sampling frequency limit.

for the simulations and the aerodynamic model is $F_{s,FAST} = 100\,Hz$. The simulation time is $T_{s,FAST} = 6400\,s$ (larger than the requirements of 10 min) to ensure statistical convergence. Global and local variables, such as thrust, torque or strain gauges on the blades can be obtained. Only the power is presented here, and the detailed analysis of the wind turbine performance is left for future work.

6.2   Results

In order to demonstrate the benefit of using the proposed method, output rotor power values obtained with the FAST simulations for different inlet flow configurations are presented in the current section. To ascertain the performance of the present approach compared with more standard techniques, the output power values of a single FOWT immersed in an atmospheric boundary layer are first presented in Fig. 11 and then compared to simulations performed using the TurbSim turbulent inflow generator available in FAST. The RMS velocity for the reconstructed TBL is around 7 % at the hub, as presented in Fig. 9. The mean power matches well for simulations with input using our experimental fields and TurbSim (Fig. 11a). A difference up to 0.3 % is observed between these mean powers with a comparable RMS velocity, in particular with $I_U = 7\,\%$. The RMS power obtained with experimental fields also matches the simulations with TurbSim datasets with similar turbulence levels. It should be

noticed that the produced power is lower than 5 MW due to the choice of the TSR.

In a second step, the ability of the present method to account for flow configurations more complex than the atmospheric boundary layer (ABL) alone is demonstrated by conducting FAST calculations of the performance of a wind turbine located in the wake of a first FOWT that is itself subjected to a surge motion. Results are shown in Fig. 12. For a fixed upstream FOWT ($F_m^+ = 0.0$), the power produced for the second turbine decreased by 87 % compared with the unperturbed turbine. This difference is consistent with the power loss found in previous studies for an array of two turbines or inside farms (Ceccotti et al., 2016; Bartl et al., 2012; Corten et al., 2004; Eecen et al., 2006; El-Asha et al., 2017). For the lowest frequency tested ($F_m^+ = 0.08$), the mean power is similar to the fixed model (less than 2 % difference). For higher frequencies ($F_m^+ > 0.11$), the calculated power drops significantly, corresponding to a decrease of $-9.4\,\%$ and $-10.3\,\%$ for surge motion frequencies of $F_m^+ = 0.11$ and 0.14, respectively. The RMS rotor power is shown to be particularly significant with respect to the mean power, approximately 50 % of $\overline{P}$ for all cases. An increase in the RMS power is shown for all surge motions compared with the fixed model. The threshold at $F_m^+ = 0.11$ observed for the mean power is also important for the fluctuating component: this increase in the RMS power is about 12 % for the lowest frequency and 4 %–5 % for higher frequencies.
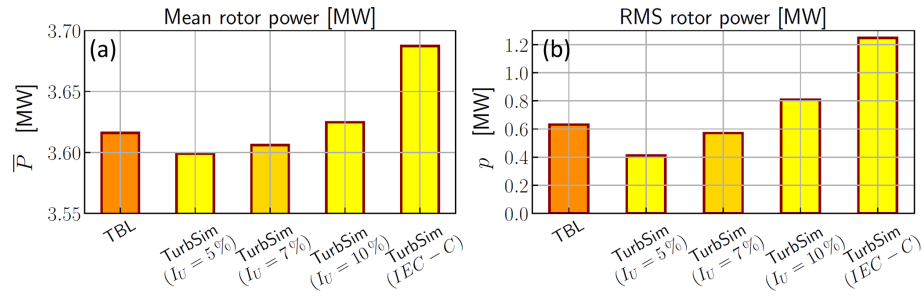
Figure 11. Comparison of the **(a)** mean and **(b)** RMS powers simulated with our experimental TBL and the wind field datasets obtained with TurbSim with four turbulence levels: $I_U = 5\,\%$, $7\,\%$, $10\,\%$ and the reference Normal Turbulence Model in IEC 61400-1 requirements (class C).
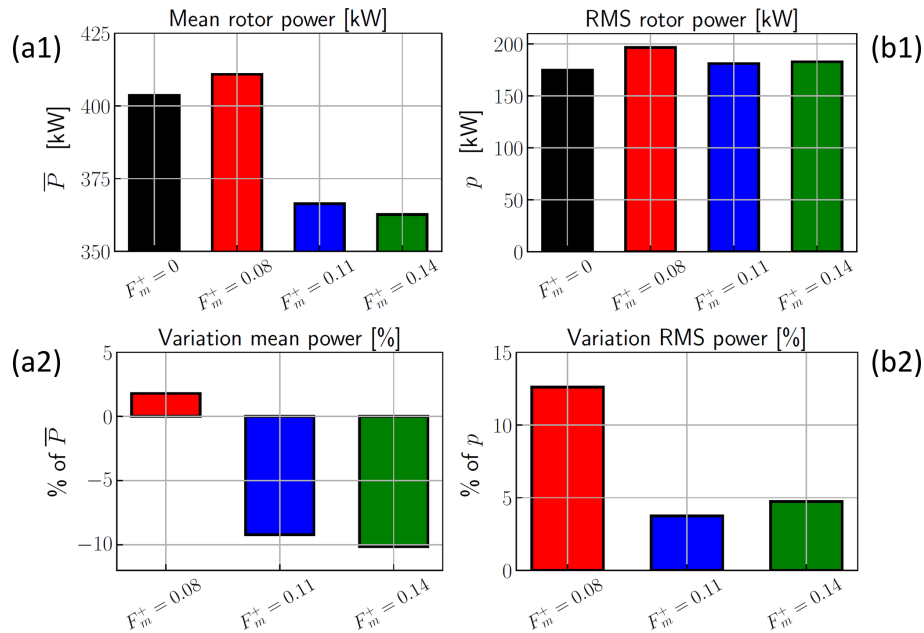

Figure 12. Effect of the surge motion on the powers obtained using QBlade/FAST simulations. The numbers 1 and 2 in the panel labels represent raw power and variation (in percent) compared with the power without surge motion, respectively. Panel **(a)** presents the mean rotor power for a second FOWT depending of the surge motion frequency; panel **(b)** is the same but for RMS rotor power.

The attention of the reader is drawn to the fact that, in this section, the FAST calculations are performed over a single full-scale period of 1 h, which is not long enough to obtain statistically significant results nor draw any definite conclusion on the performance of a wind turbine subjected to the wake of FOWT and the impact of the surge motion of the latter. To demonstrate this and the influence of the choice of the averaging period compared with the typical timescales of both the ABL and the FOWT wake, statistics of the available power (AP) directly computed from the PIV velocity fields are shown in Fig. 13. Figure 13a shows the distribution of the instantaneous AP estimated over the entire inflow database. Besides the fact that the range of variations is quite large, there is a clear trend in the median AP, with an increase with surge frequencies from 0 to $F_{\mathrm{m}}^{+} = 0.11$ and a drop for $F_{\mathrm{m}}^{+} = 0.14$. Distributions of the mean and RMS AP

estimated over 1 h periods are shown in Fig. 13b and c, respectively. The range of variation in these short-period statistics can reach 25 % of their median values. This confirms the validity of the values estimated from the FAST calculations, which are within the range of variation in the statistics. It also shows that the first identified trends due to the influence of the surge frequency (Fig. 12) are not representative and that a statistical analysis of the calculation output (which is beyond the scope of the present paper) is required to draw firm conclusions.

7 Conclusions

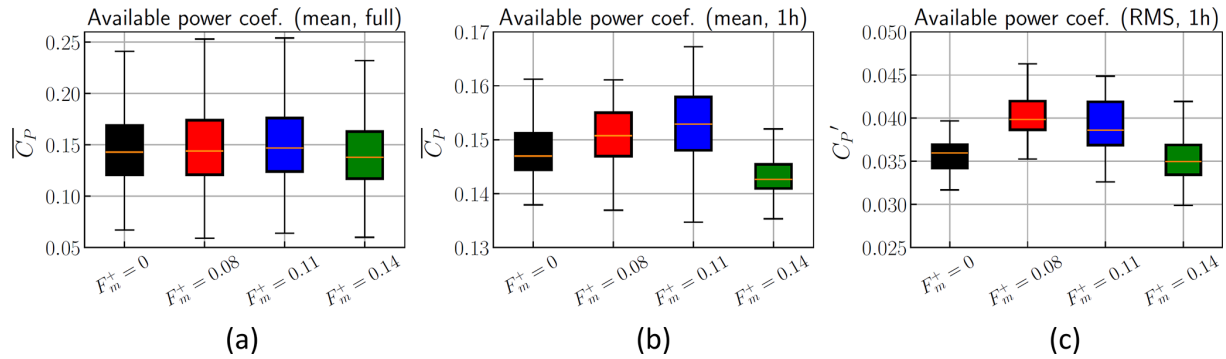A new method for generating inflow conditions for load simulations for wind turbines in complex configurations has

Figure 13. Statistics of the available normalized power computed directly from the inlet flow field. Panel **(a)** presents the available power computed using the whole database; panels **(b)** and **(c)** show the respective mean and RMS of the available power computed over 1 h periods. Box plots show the median (white), the first and third quartiles (main box), and the minimum and maximum values (whiskers).

been presented. It relies on interfacing the simulation code (FAST in the present case) with stereoscopic PIV wind tunnel measurements performed in a cross-section of the flow. This new approach has been tested in various flow configurations, including an unperturbed ABL flow and the wake of an upstream wind turbine (modeled by a porous disk in the wind tunnel) submitted to a surge motion, replicating the wave-induced movement of the FOWT platform. The incoming motion was imposed with a fixed amplitude at four different frequencies.

The boundary layer, turbulence levels and large coherent structures of the turbulent flow upstream of the model are taken into account in this study and match those of a realistic atmospheric flow. The wake was first characterized in a y–z vertical plane normal to the flow at two streamwise positions via PIV and time-resolved hot-wire anemometry. By combining the two types of measurements, velocity fields were reconstructed at a higher sampling frequency using multi-time-delay POD–LSE. The temporal POD modes showed that the horizontal meandering and the vertical downwash are part of the main dynamics of the wake; therefore, they are included in the data. The reconstructed velocities were subsequently implemented in FAST as inflow conditions to estimate the performance (using FAST) of a full-scale 5 MW wind turbine immersed in the wake of an upstream turbine subjected to a surge motion. High surge frequencies of the upstream wind turbine lead to a significant reduction in the power produced by the downstream turbine. Here, a decrease up to 10.3 % of the power for the highest frequency is observed, which needs to be confirmed in future analyses.

Coupling experimental data from wind tunnel and numerical simulations for the full-scale turbine constitutes the originality of the approach presented here. The flow conditions (in particular the boundary layer and turbulence level) and the experimental parameters (in particular the frequency of the stochastic reconstruction) were chosen to match the requirements for FAST simulations. Extrapolations were used

to adapt the velocity fields, as FAST input does not alter the mean and unsteady dynamics of the flow.

The present study focuses on a limited range of frequencies of motion in the streamwise direction. A possible improvement in the experimental setup is the consideration of all 6 degrees of freedom for the motion and to increase the frequency range for better representativity. For the stochastic tool, classical regularization techniques could help to improve the reconstruction quality. For FAST simulations, it could be interesting to consider floating wind turbines for the model to understand the interaction between the experimental input and the FOWT performance simulated by FAST.

As the spatial modes are unchanged (Fig. 6) and the physical differences are mainly contained in the temporal modes, representative velocity fields can be easily generated using a reduced set of parameters. For a low-order modeling strategy, it means that a unique set of spatial modes could be used, combined with artificial temporal modes with the proper dynamics in order to generate flow fields corresponding to generic floating wind turbines. This could allow, for example, real-time estimation of the wind turbine performance based on limited measurements on the full-scale prototype and a priori information from wind tunnel data.

lected the data. CR and JCG designed and analyzed the FAST simulations. CR wrote the basic draft of the paper. CR and LP wrote the final version of the manuscript. All authors provided critical feedback and helped shape the research, analysis and manuscript.

References

Aubrun, S., Loyer, S., Hancock, P. E., and Hayden, P.: Wind turbine wake properties: Comparison between a non-rotating simplified wind turbine model and a rotating model, J. Wind Eng. Indust. Aerodynam., 120, 1–8, https://doi.org/10.1016/j.jweia.2013.06.007, 2013.

Bartl, J., Pierella, F., and Sætran, L.: Wake measurements behind an array of two model wind turbines, Energy Procedia, 24, 305–312, https://doi.org/10.1016/j.egypro.2012.06.113, 2012.

Bastankhah, M. and Porté-Agel, F.: A new analytical model for wind-turbine wakes, Renew. Energy, 70, 116–123, https://doi.org/10.1016/j.renene.2014.01.002, 2014.

Bastine, D., Witha, B., Wächter, M., and Peinke, J.: POD analysis of a wind turbine wake in a turbulent atmospheric boundary layer, J. Phys.: Conf. Ser., 524, 012153, https://doi.org/10.1088/1742-6596/524/1/012153, 2014.

Bastine, D., Witha, B., Wächter, M., and Peinke, J.: Towards a simplified dynamic wake model using POD analysis, Energies, 8, 895–920, https://doi.org/10.3390/en8020895, 2015.

Bastine, D., Vollmer, L., Wächter, M., and Peinke, J.: Stochastic wake modelling based on POD analysis, Energies, 11, 1–29, https://doi.org/10.3390/en11030612, 2018.

Belvasi, N., Conan, B., Schliffke, B., Perret, L., Desmond, C., Murphy, J., and Aubrun, S.: Far-Wake Meandering of a Wind Turbine Model with Imposed Motions: An Experimental S-PIV Analysis, Energies, 15, 1–17, https://doi.org/10.3390/en15207757, 2022.

Betz: Das maximum der theoretisch moglichen Auswendung des Windes durch Windmotoren, Zeitschrift Für Das Gesamte Turbinenwesen, 26, 307–309, 1920.

Blackman, K. and Perret, L.: Non-linear interactions in a boundary layer developing over an array of cubes using stochastic estimation, Phys. Fluids, 28, 095108, https://doi.org/10.1063/1.4962938, 2016.

Bonnet, J. P., Cole, D. R., Delville, J., Glauser, M. N., and Ukeiley, L. S.: Stochastic estimation and proper orthogonal decomposition: Complementary techniques for identifying structure, Exp. Fluids, 17, 307–314, https://doi.org/10.1007/BF01874409, 1994.

Camp, E. H. and Cal, R. B.: Mean kinetic energy transport and event classification in a model wind turbine array versus an array of porous disks: Energy budget and octant analysis, Phys. Rev. Fluids, 1, 044404, https://doi.org/10.1103/PhysRevFluids.1.044404, 2016.

Canet, H., Bortolotti, P., and Bottasso, C. L.: On the scaling of wind turbine rotors, Wind Energ. Sci., 6, 601–626, https://doi.org/10.5194/wes-6-601-2021, 2021.

Ceccotti, C., Spiga, A., Bartl, J., and Sætran, L.: Effect of Upstream Turbine Tip Speed Variations on Downstream Turbine Performance, Energy Procedia, 94, 478–486, https://doi.org/10.1016/j.egypro.2016.09.218, 2016.

Chamorro, L. P. and Porté-Agel, F.: A wind-tunnel investigation of wind-turbine wakes: Boundary-Layer turbulence effects, Bound.-Lay. Meteorol., 132, 129–149, https://doi.org/10.1007/s10546-009-9380-8, 2009.

Chen, G., Liang, X. F., and Li, X. B.: Modelling of wake dynamics and instabilities of a floating horizontal-axis wind turbine under surge motion, Energy, 239, 122110, https://doi.org/10.1016/j.energy.2021.122110, 2022.

Corniglion, R., Harris, J., Peyrard, C., and Capaldo, M.: Comparison of the free vortex wake and actuator line methods to study the loads of a wind turbine in imposed surge motion, J. Phys.: Conf. Ser., 1618, 052045, https://doi.org/10.1088/1742-6596/1618/5/052045, 2020.

Corten, G., Schaak, P., and Hegberg, T.: Velocity profiles measured above a scaled wind farm, Energy research Centre of the Netherlands, 22–25, ftp://ftp.ecn.nl/pub/www/library/report/2004/rx04123.pdf (last access: 14 November 2023), 2004.

Cruz, J. and Atcheson, M., eds.: Floating Offshore Wind Energy, Green Energy and Technology, Springer International Publishing, Cham, https://doi.org/10.1007/978-3-319-29398-1, 2016.

De Cillis, G., Cherubini, S., Semeraro, O., Leonardi, S., and De Palma, P.: POD-based analysis of a wind turbine wake under the influence of tower and nacelle, Wind Energy, 24, 609–633, https://doi.org/10.1002/we.2592, 2021.

Dekou, R., Foucaut, J. M., and Stanislas, M.: Large scale organization of a near wall turbulent boundary layer, Int. J. Heat Fluid Flow, 61, 12–20, https://doi.org/10.1016/j.ijheatfluidflow.2016.04.005, 2016.

Dierckx, P.: An algorithm for surface-fitting with spline functions, IMA J. Numer. Anal., 1, 267–283, https://doi.org/10.1093/imanum/1.3.267, 1981.

Durgesh, V. and Naughton, J. W.: Multi-time-delay LSE-POD complementary approach applied to unsteady high-

Reynolds-number near wake flow, Exp. Fluids, 49, 571–583, https://doi.org/10.1007/s00348-010-0821-4, 2010.

Eecen, P. J., Barhorst, S. A., Braam, H., Curvers, A. P., Korterink, H., Machielse, L. A., Nijdam, R. J., Rademakers, L. W., Verhoef, J. P., Vd Werff, P. A., Werkhoven, E. J., and Van Dok, D. H.: Measurements at the ECN Wind Turbine Test location Wieringermeer, in: European Wind Energy Conference and Exhibition 2006, EWEC 2006, vol. 2, 1477–1480, ISBN 9781622764679, 2006.

El-Asha, S., Zhan, L., and Iungo, G. V.: Quantification of power losses due to wind turbine wake interactions through SCADA, meteorological and wind LiDAR data, Wind Energy, 20, 1823–1839, https://doi.org/10.1002/we.2123, 2017.

Fontanella, A., Zasso, A., and Belloli, M.: Wind tunnel investigation of the wake-flow response for a floating turbine subjected to surge motion, J. Phys.: Conf. Ser., 2265, 042023, https://doi.org/10.1088/1742-6596/2265/4/042023, 2022.

Foti, D., Yang, X., and Sotiropoulos, F.: Similarity of wake meandering for different wind turbine designs for different scales, J. Fluid Mech., 842, 5–25, https://doi.org/10.1017/jfm.2018.9, 2018.

Foti, D., Yang, X., Shen, L., and Sotiropoulos, F.: Effect of wind turbine nacelle on turbine wake dynamics in large wind farms, J. Fluid Mech., 869, 1–26, https://doi.org/10.1017/jfm.2019.206, 2019.

Frandsen, S., Barthelmie, R., Pryor, S., Rathmann, O., Larsen, S., Højstrup, J., and Thøgersen, M.: Analytical modelling of wind speed deficit in large offshore wind farms, Wind Energy, 9, 39–53, https://doi.org/10.1002/we.189, 2006.

Fu, S., Jin, Y., Zheng, Y., and Chamorro, L. P.: Wake and power fluctuations of a model wind turbine subjected to pitch and roll oscillations, Appl. Energy, 253, 113605, https://doi.org/10.1016/j.apenergy.2019.113605, 2019.

Hamilton, N., Viggiano, B., Calaf, M., Tutkun, M., and Cal, R. B.: A generalized framework for reduced-order modeling of a wind turbine wake, Wind Energy, 21, 373–390, https://doi.org/10.1002/we.2167, 2018.

Hodgkin, A., Deskos, G., and Laizet, S.: On the interaction of a wind turbine wake with a conventionally neutral atmospheric boundary layer, Int. J. Heat Fluid Flow, 102, 109165, https://doi.org/10.1016/j.ijheatfluidflow.2023.109165, 2023.

Huang, Y., Wan, D., and Hu, C.: Numerical Study of Wake Interactions between Two Floating Offshore Wind Turbines, in: Proceedings of the International Offshore and Polar Engineering Conference, June 2018, 541–548, ISBN 9781880653876, 2018.

Hultmark, M. and Smits, A. J.: Temperature corrections for constant temperature and constant current hot-wire anemometers, Meas. Sci. Technol., 21, 105404, https://doi.org/10.1088/0957-0233/21/10/105404, 2010.

International Electrotechnical Commission: Wind turbines – Part 1: Design requirements, https://webstore.iec.ch/publication/5426 (last access: 14 November 2023), 2006.

Jensen, N. O.: A note on wind generator interaction, Risø-M-2411 Risø National Laboratory, Roskilde, 1–16, http://www.risoe.dk/rispubl/VEA/veapdf/ris-m-2411.pdf (last access: 14 November 2023), 1983.

Jonkman, J., Butterfield, S., Musial, W., and Scott, G.: Definition of a 5-MW reference wind turbine for offshore system development, Tech. Rep., February, NREL – National Renewable Energy Lab., Golden, CO, USA, http://tethys-development.pnnl.gov/sites/default/files/publications/Jonkman_et_al_2009.pdf (last access: 14 November 2023), 2009.

Joukowsky, N.: Windmill of the NEJ type, Transactions of the Central Institute for Aero-hydrodynamics of Moscow, 1, 405–430, 1920.

Kaldellis, J. K., Triantafyllou, P., and Stinis, P.: Critical evaluation of Wind Turbines' analytical wake models, Renew. Sustain. Energ. Rev., 144, 110991, https://doi.org/10.1016/j.rser.2021.110991, 2021.

Kelley, N. D. and Jonkman, B. J.: Overview of the TurbSim stochastic inflow turbulence simulator: Version 1.21 (revised february 1, 2001) (No. NREL/TP-500-41137), Tech. Rep., April, NREL – National Renewable Energy Lab., Golden, CO, USA, https://www.nrel.gov/docs/fy07osti/41137.pdf (last access: 14 November 2023), 2007.

Khosravi, M., Sarkar, P., and Hu, H.: An experimental investigation on the performance and the wake characteristics of a wind turbine subjected to surge motion, in: 33rd Wind Energy Symposium, American Institute of Aeronautics and Astronautics, 1–11, https://doi.org/10.2514/6.2015-1207, 2015.

Leite, H. F., Avelar, A. C., de Abreu, L., Schuch, D., and Cavalieri, A.: Proper orthogonal decomposition and spectral analysis of a wall-mounted square cylinder wake, J. Aerosp. Technol. Manage. 10, 1–15, https://doi.org/10.5028/jatm.v10.867, 2018.

Li, Z., Dong, G., and Yang, X.: Onset of wake meandering for a floating offshore wind turbine under side-to-side motion, J. Fluid Mech., 934, A29, https://doi.org/10.1017/jfm.2021.1147, 2022.

Mann, J.: Wind field simulation, Probabil. Eng. Mech., 13, 269–282, https://doi.org/10.1016/s0266-8920(97)00036-2, 1998.

Marten, D., Lennie, M., Pechlivanoglou, G., Nayeri, C. N., and Paschereit, C. O.: Implementation, optimization and validation of a nonlinear lifting line free vortex wake module within the wind turbine simulation code qblade, in: Proceedings of the ASME Turbo Expo, 9, 15–19 June 2015, Montreal, Quebec, Canada, https://doi.org/10.1115/GT2015-43265, 2015.

Messmer, T., Brigden, C., Peinke, J., and Hölling, M.: A six degree-of-freedom set-up for wind tunnel testing of floating wind turbines, J. Phys.: Conf. Ser., 2265, 042015, https://doi.org/10.1088/1742-6596/2265/4/042015, 2022.

Nybø, A., Nielsen, F. G., Reuder, J., Churchfield, M. J., and Godvik, M.: Evaluation of different wind fields for the investigation of the dynamic response of offshore wind turbines, Wind Energy, 23, 1810–1830, https://doi.org/10.1002/we.2518, 2020.

Perret, L., Delville, J., Manceau, R., and Bonnet, J.-P.: Generation of turbulent inflow conditions for large eddy simulation from stereoscopic PIV measurements, Int. J. Heat Fluid Flow, 27, 576–584, https://doi.org/10.1016/j.ijheatfluidflow.2006.02.005, 2006.

Perret, L., Delville, J., Manceau, R., and Bonnet, J. P.: Turbulent inflow conditions for large-eddy simulation based on low-order empirical model, Phys. Fluids, 20, 075107, https://doi.org/10.1063/1.2957019, 2008.

Podvin, B., Nguimatsia, S., Foucaut, J. M., Cuvier, C., and Fraigneau, Y.: On combining linear stochastic estimation and proper orthogonal decomposition for flow reconstruction, Exp. Fluids, 59, 1–12, https://doi.org/10.1007/s00348-018-2513-4, 2018.

Porté-Agel, F., Bastankhah, M., and Shamsoddin, S.: Wind-Turbine and Wind-Farm Flows: A Review, in: vol. 174, Springer Netherlands, https://doi.org/10.1007/s10546-019-00473-0, 2020.

Raibaudo, C. and Perret, L.: Low-Order Representation of the Wake Dynamics of Offshore Floating Wind Turbines, in: 12th International Symposium on Turbulence and Shear Flow Phenomena, TSFP 2022, Osaka, Japan, 1–6, 2022.

Raibaudo, C., Piquet, T., Schliffke, B., Conan, B., and Perret, L.: POD analysis of the wake dynamics of an offshore floating wind turbine model, J. Phys.: Conf. Ser., 2265, 022085, https://doi.org/10.1088/1742-6596/2265/2/022085, 2022.

Rockel, S., Camp, E., Schmidt, J., Peinke, J., Cal, R. B., and Hölling, M.: Experimental study on influence of pitch motion on the wake of a floating wind turbine model, in: vol. 7, MDPI, https://doi.org/10.3390/en7041954, 2014.

Rousset, J.-M., Mouslim, H., Le Bihan, G., and Babarit, A.: Le projet SEM-REV : un site d'expérimentation en mer pour la recherche et l'industrie, Centre Francais du Littoral, 813–822, https://doi.org/10.5150/jngcgc.2010.090-r, 2010.

Saranyasoontorn, K. and Manuel, L.: Low-dimensional representations of inflow turbulence and wind turbine response using Proper Orthogonal Decomposition, J. Sol. Energ. Eng., 127, 553–562, https://doi.org/10.1115/1.2037108, 2005.

Schliffke, B.: Experimental characterisation of the far wake of a modelled floating wind turbine as a function of incoming swell, PhD thesis, École Centrale de Nantes, Nantes, https://theses.hal.science/tel-03722239/ (last access: 14 November 2023), 2022.

Schliffke, B., Aubrun, S., and Conan, B.: Wind Tunnel Study of a "floating" Wind Turbine's Wake in an Atmospheric Boundary Layer with Imposed Characteristic Surge Motion, J. Phys.: Conf. Ser., 1618, 062015, https://doi.org/10.1088/1742-6596/1618/6/062015, 2020.

Schmidt, J. and Stoevesandt, B.: The impact of wake models on wind farm layout optimization, J. Phys.: Conf. Ser., 625, 012040, https://doi.org/10.1088/1742-6596/625/1/012040, 2015.

Sirovich, L.: Turbulence and the dynamics of coherent structures. Part 2: Symmetries and transformations, Quart. Appl. Math., 15, 573–582, 1987.

Tarpin, G.: Physical Modelling of Floating Offshore Wind Turbines Inside a Wind Tunnel, Tech. rep., Centrale Nantes, Nantes, 2018.

VDI: Environmental meteorology – Turbulence parameters for dispersion models supported by measurement data, Tech. rep., Verein Deutscher Ingenieure, https://www.vdi.de/en/home/vdi-standards/details/vdi-3783-blatt-8-environmental-meteorology-turbulence (last access: 14 November 2023), 2017.